Structure Development during the Melt Spinning of Polyethylene and Poly(vinylidene fluoride) Fibers by in Situ Synchrotron Small- and Wide-Angle X-ray Scattering Techniques

Joshua M. Samon and Jerold M. Schultz*

Department of Chemical Engineering, University of Delaware, Newark, Delaware 19716

Benjamin S. Hsiao*

Department of Chemistry, State University of New York at Stony Brook, Stony Brook, New York 11794

Sönke Seifert

Department of Chemistry, Argonne National Laboratory, Argonne, Illinois 60439

Norbert Stribeck and Inga Gurke

Institut für Technische und Makromolekulare Chemie, Universität Hamburg, Hamburg, Germany 22603

George Collins

Corporate Research and Technology, Hoechst Celanese Corporation, Summit, New Jersey 07901

Cheng Saw

Lawrence Livermore National Laboratory, Chemistry and Materials Science Directorate, P.O. Box 808, L-350, Livermore, California 94550

ABSTRACT: In the present study, the structural and morphological development during melt spinning of polyethylene and poly(vinylidene fluoride) fibers was studied using simultaneous in-situ synchrotron small- and wide-angle X-ray scattering (SWAXS) techniques. The spinning apparatus consisted of a single screw extruder, which was mounted on a horizontal platform that could be translated in the vertical direction allowing different spinneret distances to be sampled with the X-ray beam. Effects of take-up speed (10.6–61.0 mpm) and spinneret distance (30–87.5 cm) on crystallinity and morphological parameters were investigated. A suggested model of structural development during crystallization details the formation of defective shish crystals, followed by the formation of kebob crystals. The defective shish-kebob structure eventually transforms into a well-defined lamellar structure. This model is consistent with the qualitative appearance of the two-dimensional SAXS and WAXS patterns, as well as the quantitative analysis of the SAXS/WAXS data using position-sensitive wire detectors.

Introduction

There have been great advances in the study of the structure and morphology of melt-spun polymer fibers over the past several decades. From the work of Carothers and Hill,[1] it was first noted that a process–structure–property (PSP) relationship exists in the processing of polymer fibers. This PSP relationship simply states that the processing conditions imposed on a polymer system have a large effect on the structure and morphology exhibited by polymer after processing. This alteration in structure has a direct bearing in the final properties that the polymer fiber possesses. For many of the initial experiments on this topic off-line fibers were examined. Substantial information has been gained by such postmortem examination of fibers, but the probing of structural development during processing is lost.

In 1964, Chappel and co-workers[2] made the first on-line measurements of structure development during the melt-spinning process. This was followed by the studies of Katayama et al.[3] and Spruiell, White, and co-workers.[4–9] With this work as a foundation, many polymer fiber systems were studied, including polyethylene,[3–5,9,10] polypropylene,[5,6] poly(ethylene terephthalate),[11] poly(vinylidene fluoride),[12,13] and various polyamides.[14–16] A thorough review of the orientation development and crystallization behavior during the melt spinning of polymer fibers[17] summarizes much of the work listed above.

Poly(vinylidene fluoride) [PVDF] is a ferroelectric polymer[18] whose major uses take advantage of its piezoelectric character. PVDF also finds uses as fishing line and as a material used for medical suture fibers due to its high tensile strength. It has been shown that PVDF is polymorphic[19,20] and exists in four distinct crystal phases, depending on its crystallization history.

The α-phase or form II is usually formed during crystallization from the melt. It consists of a nonpolar monoclinic unit cell resulting from the canceling of the dipoles exhibited by the two polar monomer chains that make up the cell. The conformation of the chains has been shown to be TGTG′. This crystal structure exhibits no piezoelectric characteristics. The β-phase, also known

as form I, can result from mechanical deformation of the α-phase.[21] Its unit cell is orthorhombic and consists of two nearly planar chains. This structure is piezoelectric. Form III (the γ-phase) is formed by crystallization at high temperatures or pressures or crystallization from various solutions, such as dimethyl acetamide and dimethyl sulfoxide. The γ-phase conformation has been recently shown to be TTTGTTTG′[20] and not trans zigzag as previously reported.[22] Due to its closely related structure, the γ-phase rapidly transforms into the β-phase when deformed.[22] Form IV, sometimes denoted as α_p, is the polar analogue of the α-phase and is produced by crystallization under high electric fields.

Cakmak and co-workers[12] have shown that melt spinning of PVDF fibers produces both the α and β crystalline phases. The appearance of the β-phase is stress dependent, first occurring at a spinline stress of 3 MPa and showing increased concentration as stress is increased. It was hypothesized that the β-phase resulted from a stress-induced phase transition from the melt. Small-angle light scattering (SALS) was used to investigate the superstructure. A transition from a spherulitic structure to a sheaf and rodlike structure was observed with increasing draw ratio. A later study by the above authors[13] suggested that PVDF crystallizes with a shish-kebob type morphology during the melt-spinning process. The development of this morphology was explained by the progression through two distinct regimes. In regime I, shish structures form from regions of periodic fluctuations of crystalline and amorphous polymer. In regime II a volume-filling crystallization takes place between existing shish structures, and the kebobs form from a radial overgrowth along the shishes.

The structural development of polyethylene [PE] during the melt-spinning process has been thoroughly studied over past decades by many researchers, some of which are referenced above. PE's unit cell is normally orthorhombic, but under certain conditions a hexagonal transitional phase has been reported. High-density polyethylene exhibits very rapid crystallization kinetics and very high crystallinities. The ultimate value of crystallinity has been shown to vary with the degree of branching in the polymer. It has been noted in the past[23] that PE also exhibits shish-kebob type morphology when crystallized under stress.

For both polymers listed above, it has been reported previously that SAXS reflections appear before crystalline WAXS reflections. It has been suggested that this behavior is due to a spinodal-like decomposition of the amorphous phase into material with a smoothly modulated, periodic density distribution.[24] The amplitude of the periodic modulation increases with time and temperature. This observation is a highly contested point in the current literature, and it is pointed out that the result might be a result of experimental data analysis artifacts. One such example is very small imperfect crystals that are not periodic enough on a small size scale to give rise to crystalline WAXS scattering while having periodic spacing on a larger size scale to give a SAXS pattern.

This determination of SAXS before WAXS cannot be done by merely examining the two-dimensional patterns. Care must be taken to deconvolute a trace of the WAXS pattern into its amorphous and crystalline components using the same shape amorphous peak each time. Only after deconvolution can the evolution of WAXS and SAXS patterns be compared. This is because

the SAXS signal occurs over a part of *q*-space where there is otherwise little signal, whereas the crystalline WAXS peaks appear over an amorphous hump.

In the present work, the melt spinning of PVDF and PE fibers will be studied with in-situ simultaneous synchrotron small- and wide-angle X-ray scattering techniques (SAXS/WAXS or SWAXS). The goal is to study the structure and morphological development of the two polymers during the spinning process using modern synchrotron techniques. Although this is not the first study of structure development for either polymer, the studies are warranted for a variety of reasons. The structure development during fiber spinning of PVDF, to the author's knowledge, has been studied only in the two reports listed above. Therefore, there exists the possibility that some structural development phenomenon has escaped detection. The chemical structure of PE is relatively simple, but it has been shown that there are many complex structural events that occur during the melt-spinning process, such as row-nucleated crystal growth. The added intensity of the synchrotron might be able to shed light on some finer points of existing crystallization models and theories. Also, with careful subtraction of the amorphous region of the two selected polymers, the examination of the possibility that the SAXS signal occurs before the WAXS signal will be reinvestigated.

Experimental Section

Materials. Solvay & Cie produced both the PE and PVDF used in this study. The PE is commercially known as "ELTEX E 4009" and is classified as high-density PE, having an approximate weight-average molecular weight of 140 000 g/mol. The PVDF is commercially known as "SOLEF 6010/0001", has a melt flow index of 17 (230 °C), and contains no nucleating agents. Its weight-average molecular weight is also in the range of 100 000 g/mol. Both polymers are of extrusion grade and quality.

Melt-Spinning Apparatus. The melt-spinning apparatus consisted of a 20 mm diameter single screw extruder attached to a metering pump. The extruder and metering pump were mounted on a horizontal platform that could be translated in the vertical direction with the use of a precise stepper−motor drive system. A diagram of the apparatus can be found in a previous paper[16] by the authors. The polymer was extruded through a single hole spinneret die with a diameter of 1.5 mm. Distances along the fiber ranging from 30 to 87 cm from the spinneret could be examined on the spinline using this apparatus. The shape of the main beam was rectangular, with the long axis normal to the fiber. The extruded fiber was taken up on a 19 cm diameter godet roll. A small ceramic guide and roller wheel was used to minimize fiber movement and vibration.

Synchrotron Characterization. The SAXS and WAXS measurements were performed at the Hamburg Synchrotron Radiation Laboratory (HASYLAB) at the deutsches Elektronen-Synchrotron (DESY) in Hamburg, Germany, using the double-focusing camera of the polymer beamline (A2).[25,26] The synchrotron radiation was monochromatized to 1.54 Å by Bragg reflection from a sagital germanium crystal monochromator and shaped and collimated with a cylindrical horizontal mirror in combination with a series of horizontal and vertical slit assemblies. The primary beam was rectangular in shape with approximate dimensions of 2 mm × 4 mm, with its long axis being perpendicular to the fiber direction. The primary beam intensity was monitored by an ionization chamber, and the intensity of the beam after passing through the sample was measured by a pin diode that also acted as a beamstop. The sample-to-detector distances for the SAXS and WAXS measurements were 139.5 and 8.0 cm, respectively.

The scattering patterns were corrected for fluctuations of the primary beam over time by dividing the scattered intensity

by the intensity of the primary beam. All scattering patterns were also normalized for varying collection times. Finally, SAXS and WAXS patterns of the system without a fiber sample were subtracted from the fiber patterns to correct for air and instrumental scattering.

Experimental Procedure. The temperature profile along the extruder for the PE was as follows: zone (1) (feed zone) = 150 °C, zone (2) = 160 °C, zone (3) = 170 °C, and zone (4) (die and metering pump) = 170 °C. The temperature profile along the extruder for the PVDF was zone (1) = 190 °C, zone (2) = 200 °C, zone (3) = 210 °C, and zone (4) = 210 °C. The extruder throughput rates for PE and PVDF were 8.0 and 11.2 g/min, respectively. These constant extruder throughputs were reached by rotating the metering pump at 8.6 rpm in each case.

SAXS and WAXS data collection was handled in two different ways. First, two imaging plates were used to capture two-dimensional images. Collection times were varied to maximize the collected intensity, but care was taken to not saturate the imaging plate. Typical collection times were 30 s for the WAXS images and 120 s for the SAXS images. After collection, the image was digitized with a resolution of 176 μm/pixel, using a Molecular Dynamics scanning workstation.

The second detection method involved the simultaneous use of a two-dimensional 256 × 256 channel wire detector to collect SAXS images and a one-dimensional position-sensitive wire detector (512 channels) to record a slice of WAXS data. This 1D detector was positioned vertically along the meridian while collecting PE data and was rotated to lie along the equator during PVDF data collection. The reason for this arrangement will be discussed later. The collection time for both the 2D and 1D detectors was 300 s. The 1D detector measured 30 10 s images (total 300 s), which were subsequently averaged into a single 10 s mean image. The patterns from the imaging plates were used mainly for qualitative analysis due their high spatial resolution and large dynamic range. On the downside, the imaging plates can be affected by outside variables such as exposure to light and human errors with image orientation. To counteract these effects, the wire detector data were used for quantitative analysis because the polymer scattering in this case is not as clouded by outside effects.

Take-up speeds of 10.6, 21.4, 28.6, 39.4, and 61.0 mpm were examined in this experiment. In addition, a fiber sample taken from the godet roll after complete crystallization was reexamined. This sample will be referred to as the "off-line" sample.

Data Analysis Techniques. 1. WAXS. The one-dimensional (1D) crystallinity index of the fibers was determined by taking the one-dimensional WAXS profiles from the 1D wire detector and, after all corrections have been made (beam intensity, collection time, subtraction of air background), curve-fitting the intensity vs 2θ (scattering angle) plot using a peak deconvolution package (Grams32 v.4.01). Since the amorphous and crystalline peaks overlapped in the equatorial (or meridional) slice, it was necessary to find the peak parameters of the amorphous peak independently. The peak parameters of the amorphous peak for the on-line patterns were determined by the fitting of the one-dimensional equatorial slice of a two-dimensional WAXS pattern taken at a distance very close to the spinneret where crystallization had yet to begin. The amorphous peak was taken to be a single Gaussian peak based on experimental observations. The center position and full width at half-maximum (fwhm) of the amorphous peak from this fit were used in all subsequent fits for the on-line patterns where crystallization had taken place.

For these on-line crystalline patterns, a peak representing the amorphous contribution was inserted with the above parameters, and its height was adjusted so that the tails of the amorphous peak fit very well with the experimental data. It is assumed that any scattering in these regions is only from the amorphous phase. At this time, various crystalline peaks were inserted, and their peak parameters (position, height, fwhm) were iterated to achieve a good fit with the experimental data. For the on-line study, these crystalline peaks were fitted with Lorentzian peaks, which fit the peaks most accurately.

After fitting the pattern with an amorphous and several crystalline peaks, the 1D crystallinity index was determined

as follows:

$$\chi_c = \frac{\sum A_C}{\sum (A_C + A_A)} \tag{1}$$

where A_C is the integrated area underneath the crystalline peaks and A_A is the integrated area of the amorphous peak of the one-dimensional slice. The upper range of integration was approximately 40° 2θ. This 1D crystallinity index can be used to compare samples within this experiment for qualitative trends but should not be considered the absolute crystallinity of the sample. These results were compared with the two-dimensional (2D) crystallinity index as calculated by applying eq 1 to a radial integration of the WAXS profiles at a series of equispaced azimuthal angles from the imaging plate after all corrections have been made.

2. SAXS. To examine the interlamellar structure, the one-dimensional correlation function method was used, as proposed by Strobl and Schneider.[27] In the one-dimensional correlation function analysis, it is assumed that the lamellar stacks are infinite in height and are perfectly oriented. The scattering from such a theoretical stacking would be a pair of discrete peaks along the stacking direction. In actuality, this scattering due to lamellae is broadened azimuthally due to the stacks not being exactly parallel to each other. Therefore, the scattering does not appear as a discrete spot but rather is spread over a section of the reflecting sphere in reciprocal space whose area is proportional to q^2. A Lorentz correction is conventionally used to correct to the value that would be seen for the perfectly oriented case in the case of the extraction of a 1D meridional slice of SAXS data.

When the 2D SAXS pattern is projected upon the meridian using the following algorithm, as done in this experiment, no Lorentz correction is needed for the integrated intensity.

$$\bar{I}(q_z) = \int_0^\infty I(q_r, q_z) q_r \, dq_r \tag{4}$$

where q_r represents the scattering vector along the equatorial direction, q_z represents that along the meridional direction, and $\bar{I}(q_z)$ is termed the projected intensity on the meridian. The scattering vector is defined as follows.

$$q = \frac{4\pi}{\lambda} \sin \theta \tag{5}$$

where λ is the X-ray wavelength and θ is one-half the scattering angle (2θ). From this point on we will replace q_z with q for simplicity.

The correlation function is calculated as

$$\gamma(r) = \frac{\int_0^\infty \bar{I}(q) \cos(qr) \, dq}{Q} \tag{6}$$

where $\bar{I}(q)$ is the integrated intensity of the 1D meridional projection and Q is the invariant, which is defined as

$$Q = \int_0^\infty \bar{I}(q) \, dq \tag{7}$$

The invariant defined in eq 7 should be classified as a "relative" invariant as opposed to an "absolute" invariant. That is to say, the values of Q calculated could be affected by parameters that were not taken into account during the experiment. One such parameter was fiber diameter. As a volume element travels from the spinneret, the diameter of the element decreases. This reduction in diameter would lead to a decrease in scattering volume and thus a decrease in Q. Since both the PE and PVDF experiments use the same processing apparatus (spinneret die, screw speed, etc.), it is assumed that the spinline diameter decreases for each to a similar degree. It is further assumed, on the basis of results stated below, that the effect of the decreasing diameter does

Distance from Spinneret (cm)

| 57.5 cm | 70.0 cm | 72.7 cm | 75.0 cm | 86.5 cm |
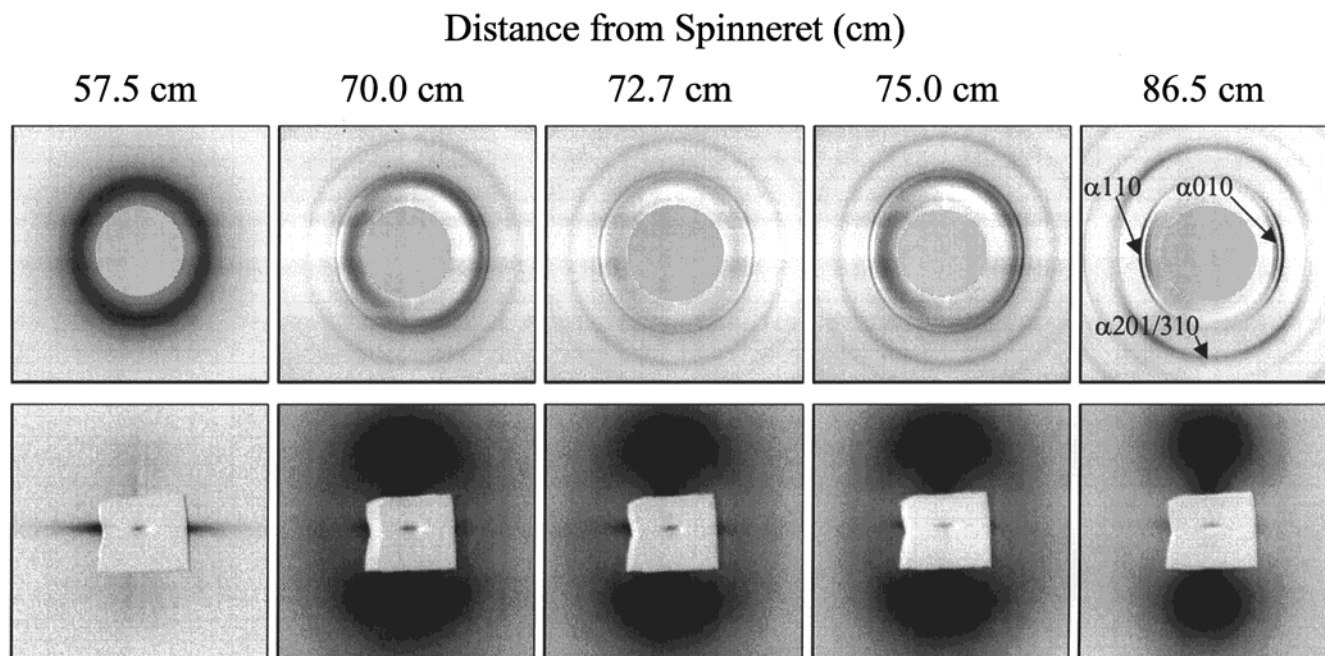
Figure 1. Two-dimensional SAXS and WAXS images for a variety of spinneret distances at a take-up speed of 10.6 mpm for poly(vinylidene fluoride) (PVDF).

not decrease Q to a qualitatively overwhelming degree, since an increase of Q is seen upon crystallization for both polymers studied.

In eqs 6 and 7, the integration on q, as stated, should be carried out between zero and infinity. Since this range is too large to be covered experimentally, the integration can be divided into three different regions. For example, eq 7 can be rewritten as[28]

$$Q = \int_0^{q_1} \bar{I}(q)\, dq + \int_{q_1}^{q_p} \bar{I}(q)\, dq + \int_{q_p}^{\infty} \bar{I}(q)\, dq \qquad (8)$$

where the detector minimum and maximum q values are q_1 and q_2, respectively. The corrected intensity data for the first integral can be found by extrapolating the corrected experimental data linearly back from q_1 to zero angle. The intensity for the second integral is the corrected intensity calculated from the observed data by integration of a projection of the two-dimensional SAXS pattern onto the meridian. The third integral's integrand is calculated by Porod's law with q_p being the beginning of the Porod region ($q_p < q_2$). In this region the data were extrapolated on the basis of Porod's law, where the integrated intensity decays as the scattering vector to the second power. This extrapolation was carried out to a scattering vector where the intensity was reduced to very close to a zero value.

The correlation function, $\gamma(r)$, is a measure of the electron density in the lamellar stacks. The value of the first peak maximum corresponds with the long period (L_{cf}). It is impossible from this analysis alone, however, to determine whether the lamellar thickness corresponds to the amorphous or crystalline thickness. Other aspects of the data must be analyzed to determine the proper assignment of the lamellar thickness.

Results and Discussion

Qualitative Analysis of 2D Patterns. Figure 1 shows a series of simultaneous SAXS and WAXS images taken for PVDF over a range of spinneret distances for a given take-up speed. Qualitatively, at very close distances to the spinneret, the WAXS pattern shows only an amorphous halo, at which time a SAXS pattern is not evident. Further from the spinneret, a strong equatorial streak and weak meridional streak develop in the SAXS pattern, while the WAXS image still only shows an amorphous halo (57.5 cm, for example). Continuing further along the spinline, the WAXS pattern begins to exhibit crystalline reflections. Simultaneously, the equatorial streak in the SAXS patterns begins to disappear and a two-lobe meridional pattern becomes dominant. Still further along the spinline, the crystalline peaks in the WAXS pattern grow stronger while the equatorial streak vanishes entirely from the SAXS pattern.

In all but the fastest take-up speed examined (61 mpm), the β-phase of PVDF was not present, and the crystalline pattern arose entirely from α-phase scattering. At 61 mpm a very weak reflection from the $\beta 010$ crystal plane was present, but due to its extremely low intensity, it does not contribute significantly to the total crystallinity of the sample.

Figure 2 shows a series of simultaneous SAXS and WAXS images taken for PE over a range of distances from the spinneret for a given take-up speed. Initially, the results look similar to those of PVDF as discussed above. At small distances from the spinneret the WAXS patterns consist of an amorphous halo while no additional scattering is noted in the SAXS patterns. At larger distances from the spinneret (such as 50 cm), as with PVDF, an equatorial streak develops without the appearance of crystalline WAXS reflections. At these take-up speeds, as one progresses further from the spinneret, the SAXS pattern develops a meridional streak (which appears differently than the meridional lobe in PVDF) while the equatorial streak begins to diminish in intensity and moves toward the beamstop. By a distance of 65 cm from the spinneret, crystalline reflections are then seen as the 110 reflection (a four-point pattern that is off equator) and a near isotropic reflection which possibly could be from a metastable hexagonal crystalline phase. Still further along the spinline, the equatorial SAXS streak disappears and the meridional streak grows in intensity. The 110 reflection appears as a four-point pattern that is off the equator, and the 200 reflection appears oriented on the meridian
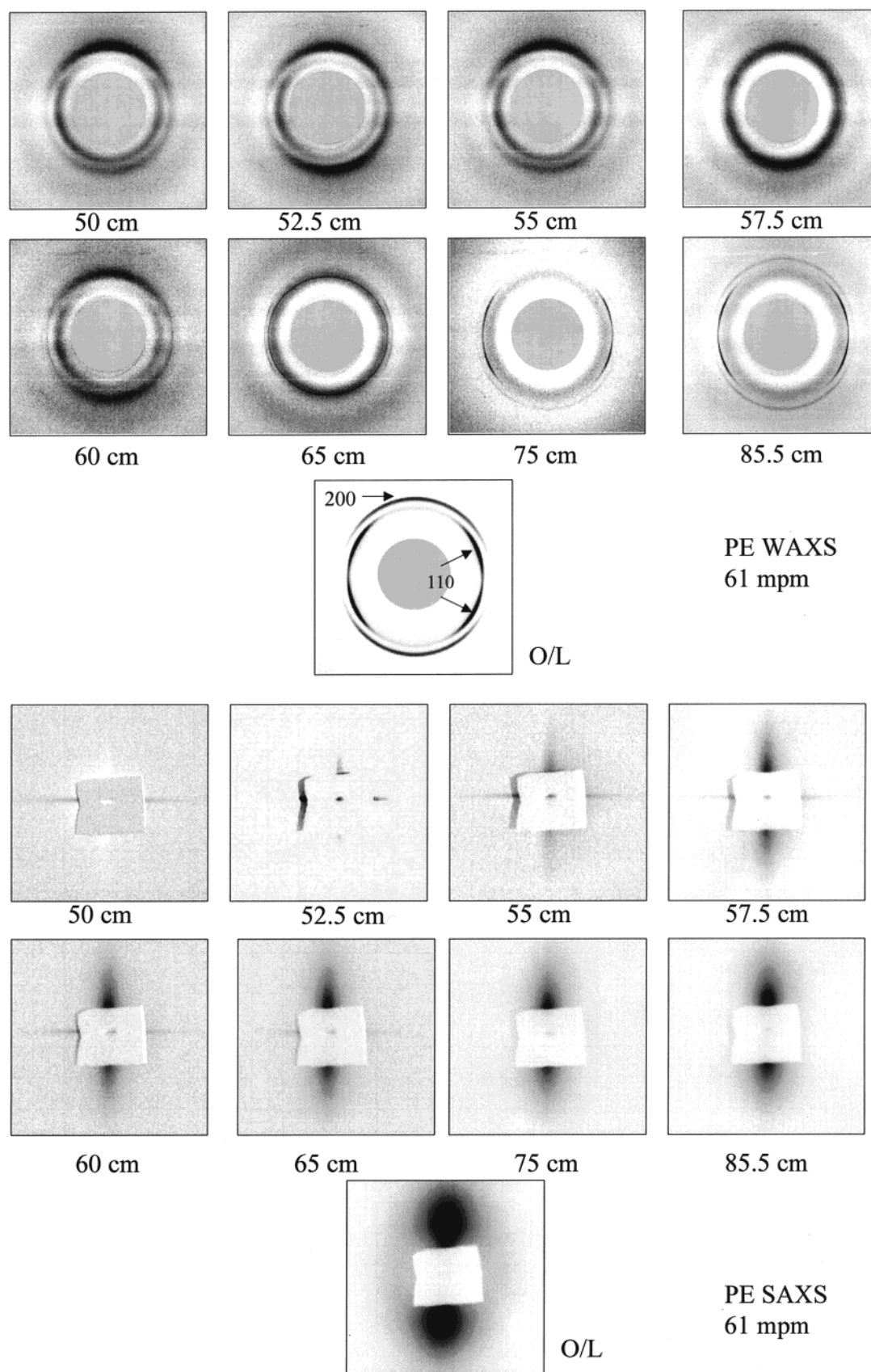
Figure 2. Two-dimensional SAXS and WAXS images for a variety of spinneret distances at a take-up speed of 61.0 mpm for polyethylene (PE).

while the scattering from the metastable phase vanishes. In examination of the off-line sample, the SAXS pattern has developed into a two-lobe pattern along the meridian and in the WAXS patterns the 200 reflection

is still aligned on the meridian, and the 110 reflection still is aligned off-equatorially in a four-point pattern. The azimuthal angular position of the maximum intensity of this off-equatorial 110 reflection decreases with
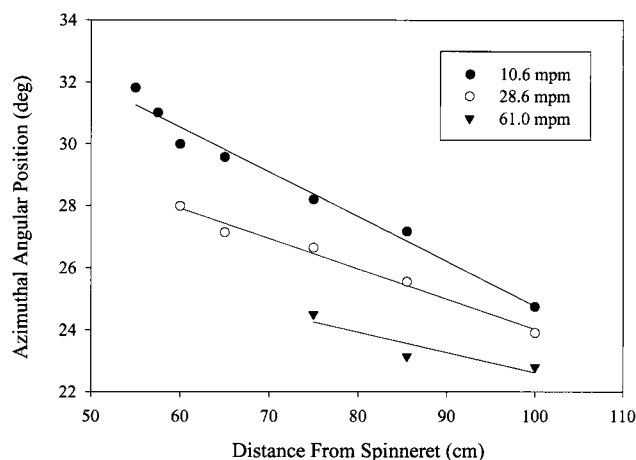
Figure 3. Azimuthal angular position of the off-equatorial 110 reflection of PE as a function of take-up speed and distance from the spinneret.

increased take-up speed (at a constant distance from the spinneret). There is also a near-linear dependence of this angular position on distance from the spinneret. These results are illustrated in Figure 3.

The meridional streak seen initially for the case of PE is still thought to be a result of a lamellar stacking of kebobs. The long period however is sufficiently large to cause the Bragg peak maximum to occur at an angular position which overlaps with the beamstop. As the distance from the spinneret increases, this long period is thought to decrease, thus causing the SAXS peak maximum to initially move away from the beamstop along the meridian. This initial decrease of long period with time has been seen, for instance, in the case of PEEK.[29] In that study it was concluded that the sharp initial decrease is either due to insertion of additional lamellae within a primary lamellar stack or crystallization producing thin lamellar stacks within pockets of amorphous polymer. Although the SAXS method cannot distinguish between the two conclusions directly, additional results seem to indicate the latter as the cause of the decrease in long period.

The authors have considered the possibility that the horizontal and vertical streaks in the SAXS patterns for both PE and PVDF could be caused by slit scattering from the collimation device. The absence of any streaks in the air background patterns (not shown) verifies that no slit scattering was present during these experiments.

The appearance of the four-point WAXS reflection of the 110 crystal plane and the meridional 200 reflection both have been observed previously[4,10] and were rationalized by the claim that there is *b*-axis radial symmetry exhibited in the fiber. In this geometry, the *b*-axis is perpendicular to the fiber axis while the *a*- and *c*-axes are oriented randomly around the *b*-axis. In one of the above works,[10] the *b*-axis radial azimuthal intensity distribution was constructed using a stereographic projection analysis,[30] and the points of intersection satisfying both the Bragg relation and the angular relation between the respective reflection plane and the fiber axis were noted. Given perfect equatorial alignment of the *b*-axis, the maximum value of the 110 reflection arcs is at a value of 33°40′ from the equator. Experimentally, these reflections were found to be nonsymmetric, fading gradually toward the equator, and past this maximum point there can be no intensity for the case of perfect alignment. Any divergence, however,

of the *b*-axis around the radial plane would cause an extension of the arcs to higher angles. Also from the stereographic projection, the 200 reflection is spread azimuthally, centered on the meridian, as seen in the WAXS patterns.

This *b*-axis orientation can stem from a row nucleated shish-kebob morphological model as described by Keller and Kolnaar.[31] Crystallization induced by the orientation effects of the extensional flow of the melt-spinning process induces crystallization of extended-chain crystals into a fibrillar form oriented with the chain axes aligned along the direction of stress. The structures are known as the "shishes" of the model. Upon a relaxation of the stress on the fiber, the amorphous material between the shish crystals can crystallize as platelet overgrowth perpendicular to the shish direction. These platelets are known as the "kebobs". Under a very weak orientation influence, the shish structures are very far apart, and as the kebobs grow they twist as they would in spherulitic growth under quiescent condition, but now only in directions normal to the shish. The *b*-axes are oriented perpendicularly to the shishes in the direction of twisting kebob growth. Because of the twisting, the *a*- and *c*-axes achieve random orientation around the *b*-axis.

The degree of randomness of the orientation of the *a*- and *c*-axes around the *b*-axis is a function of the distance between the adjacent shish structures which, in turn, is a function of the stress on the polymer fiber. It is suggested that as the spinline stress is increased, the nucleation rate of shishes is enhanced and the spacing between the shishes decreases. This is because the increase in chain orientation coverts more amorphous polymer to the shish structures, which causes the proximity of the shish structures to decrease. This allows less room for the twisting of kebobs to occur and results in less rotation of the *a*- and *c*-axes from their initial settings (*c*-axis always parallel to the fiber axis).

In the case of either polymer studied, the SAXS patterns roughly go through similar stages: equatorial streak, equatorial and meridional streaks with progressive weakening of equatorial streak, meridional streak (or lobe) with absence of equatorial streak, and finally meridional two-lobe pattern indicative of lamellar structure. The two-lobe pattern appears sooner in the case of PVDF as compared to PE. WAXS crystalline peaks appear at some time after the meridional streaks begin to appear in both cases.

The following structural model can possibly explain the above observations. First, the shish structures form and are oriented along the fiber axis. The shishes manifest themselves as an equatorial streak. These shish are very defective in three-dimensional ordering and therefore do not show crystalline reflections in the WAXS pattern. As kebobs start to grow perpendicular to the shish, a meridional streak (lobe) becomes evident. At this stage, the crystal structure in the shishes and kebobs likely becomes more perfect, and WAXS crystalline peaks are now seen. Now consider two adjacent shish kebobs growing together. Since the crystallographic axis parallel to the chain axis is *c*, the *a*- and *b*-axes are distributed randomly over the population of shishes due to the kebobs twisting during growth. Thus, as the adjacent kebobs impinge on each other, their *c*-axes are parallel but the *a*- and *b*-axes can point in different directions in the two kebobs. Consequently, there is a grain boundary, which forms between the two

impinging kebobs, and this carries with it a positive energy (stress). The grain boundary can be minimized only if the kebobs grow together. In order for them to grow together, one or both have to rotate about the *c*-axis, to align the *a*- and *b*-axes in the two kebobs. This is impossible, however, because the shishes threading through these kebobs have specific *a*–*b* orientations and cannot rotate. Therefore, the only possible way for the kebob orientation match is for the shish to be locally destroyed, and then kebob rotation is free to occur. As these shishes begin to be destroyed, the equatorial streak's intensity diminishes, and as most of the shish structures disappear, so does the equatorial streak. The morphology has now changed from shish kebob to lamellar, and a two-lobe pattern is now evident. This phenomenon has been observed via transmission electron microscopy by one of the authors previously[32] in a system of isotactic polypropylene.

Appearance of SAXS before WAXS. As seen in Figures 1 and 2 (PVDF and PE), as one moves away from the spinneret there was a distance at which a SAXS signal was detected while the WAXS pattern still exhibited an amorphous halo. This has been noted recently by other researchers in poly(ethylene terephthalate)[33] [PET], isotactic polypropylene[34] [i-PP], poly-(ether ketone ketone)[35] [PEKK], and poly(vinylidene fluoride) [PVDF][13] systems. The results of these and other experiments have been the basis of theoretical work[24] on the mechanism of this crystallization phenomenon at initial stages.

A long-range density fluctuation in the polymer melt is suggested as the driving force of the above observation. This density fluctuation results from the spinodal decomposition of the melt into domains of higher and lower electron density, giving rise to a SAXS reflection. It was previously proposed that these regions of differing density are created by the migration of conformational defects along the axes of the chains oriented along the flow axis. Regions of defect clustering have a low density, while the regions from which the defects migrated have a higher density.[36] The domain with a higher density tends toward chains in an all-trans conformation, giving rise to a more ordered structure that is the precursor to the crystalline phase. The domain of lower density contains a high concentrations of gauche bonds; this will become the amorphous region after crystallization commences. Eventually the regions of lowest conformational defect density provide crystallization sites for growth transverse to the chain axis. Once crystallization has begun, crystallization progresses and a lamellar morphology forms. In this model there is a slow and continuous transformation from oriented amorphous melt to the crystalline structure occurring during a diffusional process which is based on the axial migration of conformational defects and thus on the migration of electron density. This is in opposition to Strobl,[37] who acknowledges the results of the above experiments but, with only few examples of such behavior, generalizes that the crystal structure appears instantaneously and crystallization proceeds in a mechanism of spherulitic nucleation and growth.

The results of the experiments in the current study indicate and reconfirm that for the cases of PE and PVDF a SAXS signal appears prior to any identifiable WAXS crystalline reflections. This is illustrated in Figure 4, which shows both 1D and 2D wire detector results for two typical take-up speeds (28.6 and 21.4
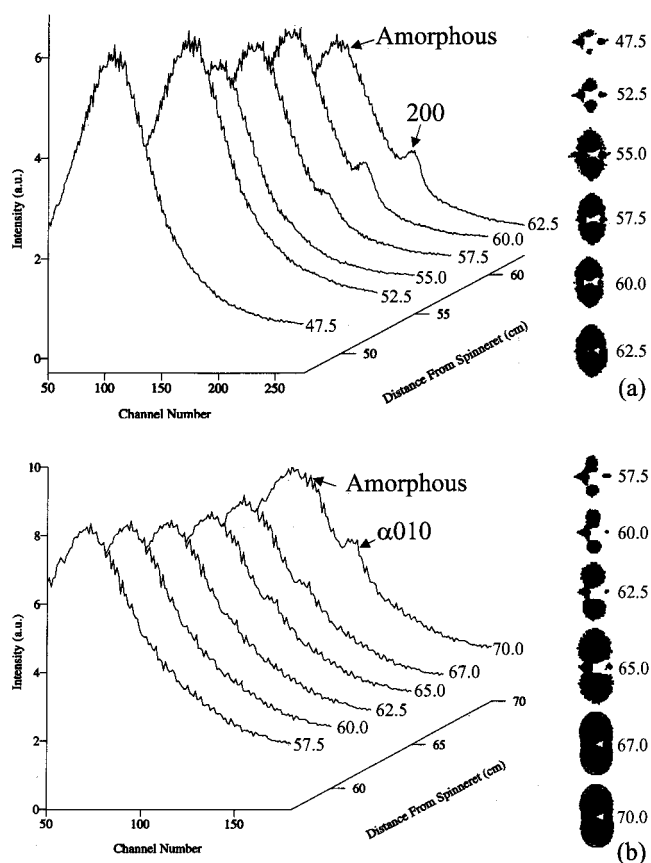
Figure 4. 1D and 2D wire detector results illustrating SAXS signals appearing before WAXS signals for (a) PE at a take-up speed of 28.6 mpm with the 1D WAXS detector positioned on the meridian and (b) PVDF at a take-up speed of 21.4 mpm with the 1D WAXS detector positioned on the equator.

mpm) for PE and PVDF, respectively. The data were normalized by the beam fluctuation, sample adsorption, and instrumental and background scattering and thus are suitable for quantitative analysis. For PE at a distance of 55 cm from the spinneret, a small shoulder appears in the meridional scan (the detector orientation is aligned along the fiber axis), indicating the appearance of the 200 crystalline reflection, while a well-defined two-lobe SAXS pattern is apparent at a distance of 52.5 cm. Likewise, for PVDF, a small shoulder appears in the equatorial scan (the detector orientation is perpendicular to the fiber axis) at a distance of 62.5 cm, indicating the α010 crystalline reflection, while the well-developed SAXS pattern is seen at 57.5 and 60.0 cm. Both of these results illustrate a SAXS signal (equatorial streak and meridional lobe) appearing before the WAXS signal. This observation appears to favor the spinodal decomposition mechanism rather than the spherulitic nucleation and growth mechanism.

However, a further comparison between the kinetics of the equatorial streak and that of the meridional streak suggests a different story, which has been seen in our earlier discussion. As the equatorial streak always appears prior to the meridional streak (lobe), we believe that the mechanism of the shish and kebob formation (discussed earlier) prevails. It is conceivable that the crystal ordering in the early stage of the crystals (shish and/or kebob) is simply too weak to be detected by the WAXD techniques, but the density fluctuations of different structures (shish and kebob) are readily detectable by SAXS.
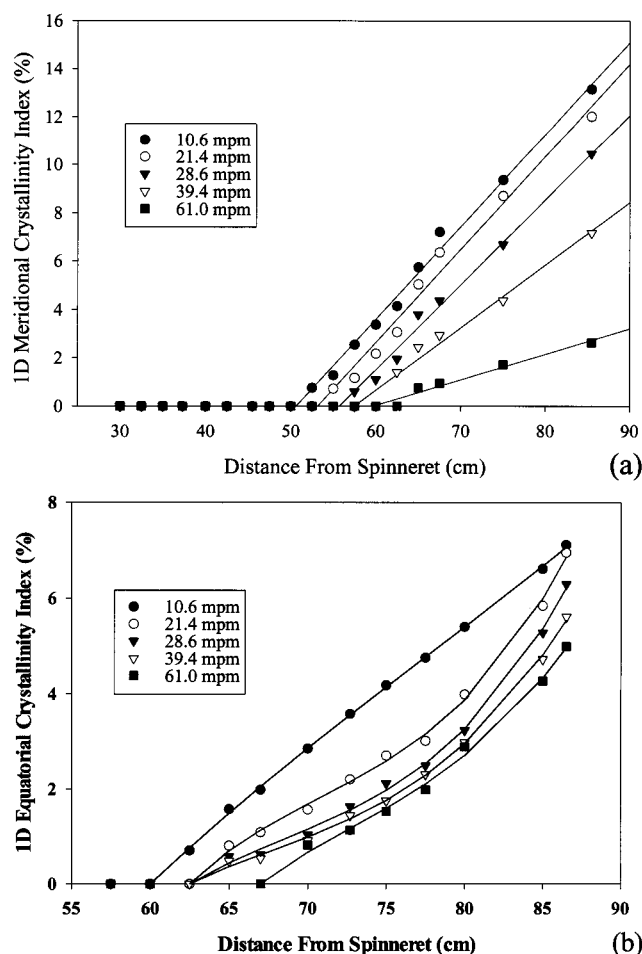
Figure 5. One-dimensional crystallinity indices for (a) PE and (b) PVDF as calculated from the 1D wire detector data. The detector was positioned equatorially for PVDF and meridionally for PE.

WAXS Crystallinity Indices (One- and Two-Dimensional).

The one-dimensional crystallinity index was calculated from a 1D wire detector which was positioned along the equator for PVDF and along the meridian for PE during the melt-spinning experiment. For the PVDF measurement, the detector position monitors the crystallinity index resulting from the α010 reflection. This reflection appeared to be very intense and therefore was a proper way to monitor the crystallinity index of the specimens in the given positions. As stated above, the polymorphic behavior of PVDF can be neglected at these low take-up speeds. For the PE experiments the 1D wire detector was positioned along the meridian to detect the 200 crystal reflection. This reflection was strong and was a good way to detect crystallinity in the sample.

Figure 5 shows the one-dimensional crystallinity index for PVDF and PE as calculated from eq 1 as a function of take-up speed and distance from the spinneret. The 1D crystallinity index remains at zero value until a specific spinneret distance where crystallization begins. This onset of crystallization point is a function of take-up speed with the crystallization beginning closer to the spinneret for lower take-up speeds and further away from the spinneret at higher take-up speeds. As crystallization proceeds, the 1D crystallinity index increases approximately linearly with distance. At a specific distance from the spinneret, lower take-up speeds possess a higher degrees of crystallinity index
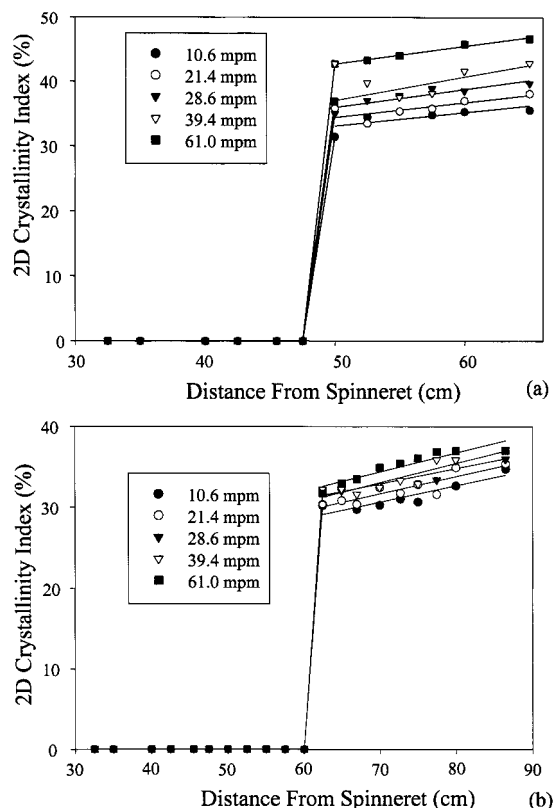

Figure 6. Two-dimensional crystallinity indices for (a) PE and (b) PVDF as calculated from WAXS imaging plates. Because of changing experimental conditions, only the trends in crystallinity are relevant.

as compared to higher take-up speeds. During the melt spinning of polymer fibers, there are two effects that influence the crystallization kinetics of the fiber: the molecular strain and the cooling of the fiber. We believe that at these low take-up speeds the molecular strain has not reached a value to cause strain-induced crystallization and thus may not warrant consideration. Thus, the main influence on the crystallization kinetics results from the cooling of the fiber as crystallization is occurring. This provides a basis to rationalize our results. At higher take-up speeds, the fiber passed more quickly from the spinneret to the X-ray beam position as compared to the lower take-up speeds. This means that the fiber will have less elapsed time to crystallize, since the fiber will have less time to cool. Faster take-up speeds, therefore, will possess lower degrees of crystallinity at a specific distance from the spinneret.

Figure 6 shows the two-dimensional crystallinity index as calculated from the radial scans of the corrected WAXS imaging plate patterns as a function of take-up speed and distance from the spinneret for both PVDF and PE fibers. Because of differing experimental conditions, i.e., temperature of the experimental hutch (the temperature during the 1D PSD measurements was generally higher since no hutch door opening was needed), results from the image plates and results from the wire detectors can be compared only for physical trends. The magnitude of the crystallinity indices or the respective onsets of crystallization for the two cases cannot be compared directly. These results are provided in order to illustrate that not only is the 1D crystallinity index increasing, but the 2D crystallinity index increases slightly as well. This acknowledges that the increase in 1D crystallinity index is due to not only an
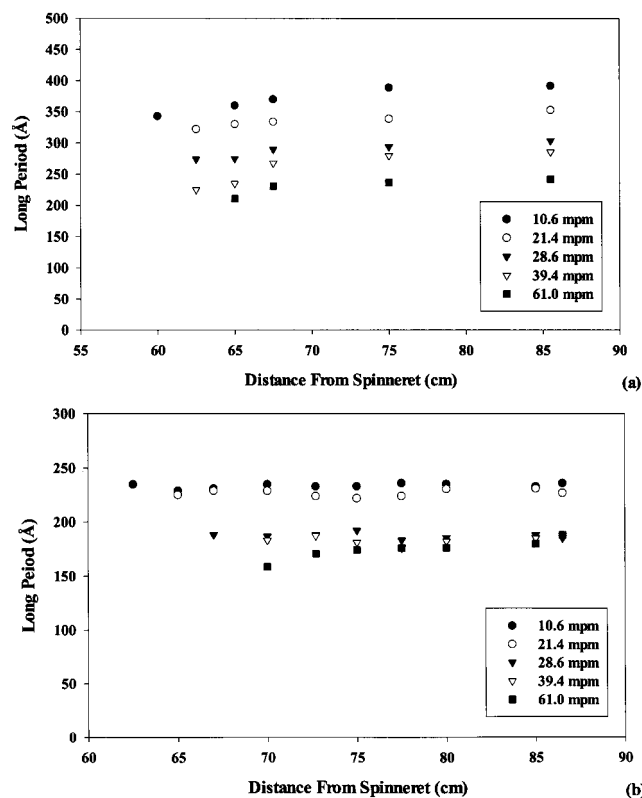
Figure 7. Long period of (a) PE and (b) PVDF as calculated by the one-dimensional correlation function from the meridionally projected 2D SAXS data from the 2D wire detector.
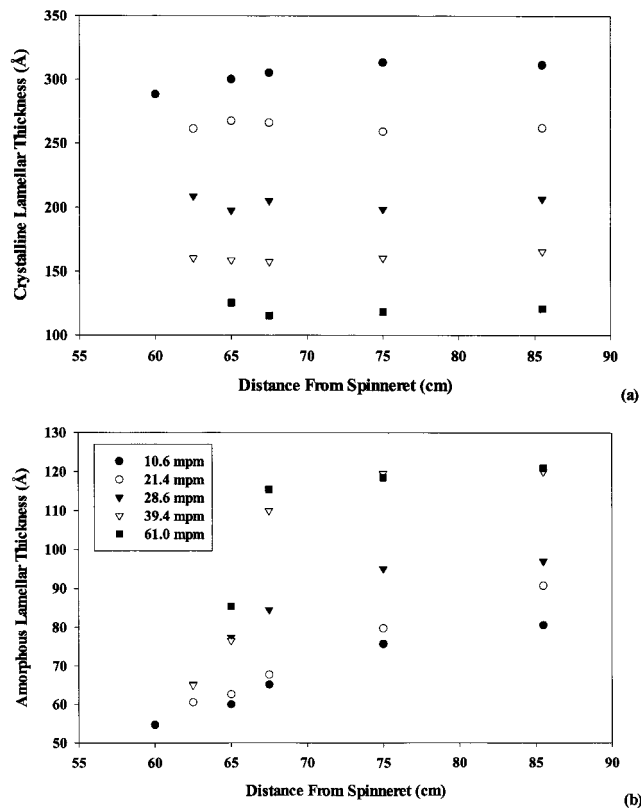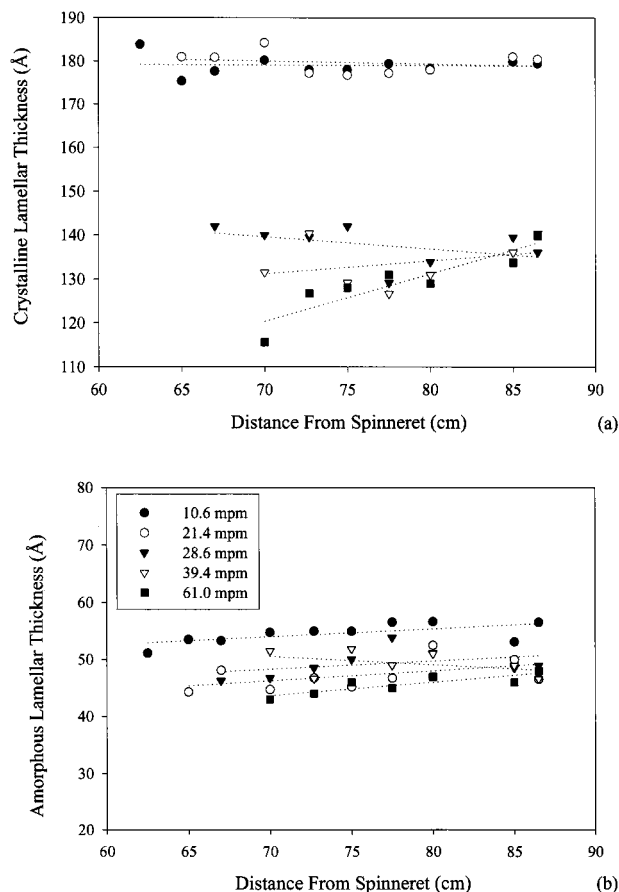

Figure 8. (a) Crystalline and (b) amorphous thicknesses of PE as calculated by the one-dimensional correlation function from the meridionally projected 2D SAXS data from the 2D wire detector.

increase in crystalline orientation but also a true increase in crystallinity.

Quantitative Analysis of 2D SAXS Patterns. Figure 7 shows the long period of the PE and PVDF as a function of take-up speed and distance from the spinneret, which is calculated from the one-dimensional correlation function analysis method of a meridional projection of the two-dimensional SAXS data as recorded by a 2D wire detector. After the onset of crystallization, the long period remains relatively constant, in the case of PVDF, or slowly increases, in the case of PE, as a function of distance from the spinneret. Slower take-up speeds exhibit larger long periods, and conversely smaller long periods are indicative of faster take-up speeds.

Figures 8 and 9 show the crystalline and amorphous thicknesses for PE and PVDF, respectively. The designation of the crystalline and amorphous thicknesses was made on the basis of the estimation of the total crystallinity of the sample after crystallization has been completed. After crystallization is completed, the samples appear to be comprised of mainly crystalline portions. Therefore, the larger lamellar thickness should correspond to the crystalline thickness and the smaller to the amorphous thickness.

For the case of PE, slower take-up speeds result in larger crystalline lamellae and smaller amorphous lamellae. After the onset of crystallization, the crystalline thickness remains almost constant while the amorphous thickness value increases steadily as one goes to further from the spinneret. The magnitude of the crystalline thickness is always greater than the value of the amorphous thickness for a given spinneret distance, and the values of both are heavily dependent on the take-up speed. By 87.5 cm from the spinneret,

the crystalline thickness is reduced by more than 50% by a comparison of the two extreme (10.6 and 61.0 mpm) take-up speeds studied in this experiment. Over this range of take-up speeds at the same spinneret distance, the amorphous thickness increases by approximately 35% from its smallest value seen at a take-up speed of 10.6 mpm.

Unlike the above, the crystalline and amorphous thicknesses of PVDF do not vary greatly with spinneret distance. The slower take-up speeds have the larger crystalline thicknesses just as in the PE fibers. However, there appears to be no strong dependence of amorphous thickness with take-up speed. The slower take-up speeds seem to possess a larger amorphous thickness, but with such small differences, all take-up speeds studied have very similar values of amorphous thickness. The crystalline thickness also shows less of a variation with take-up speed. From the largest crystalline thickness, found at a take-up speed of 10.6 mpm, the long period drops by only approximately 15% to the 61 mpm crystalline long period value. Comparatively, the decrease in PE over the same take-up speeds is about 3 times greater.

From the above, it is obvious that, in the range of take-up speeds examined, the morphology of the PE is more sensitive than PVDF to small stress changes. The PVDF does not exhibit significant variations in long period, crystalline thickness, or amorphous thickness as small stress changes are imposed on the cooling fiber. It is suggested that larger stresses (higher take-up speeds) are needed to see the same effects viewed in PE.

The dependence of the long period and crystalline lamellar thickness on take-up speed is related to the more rapid rate of cooling with increasing take-up speed.
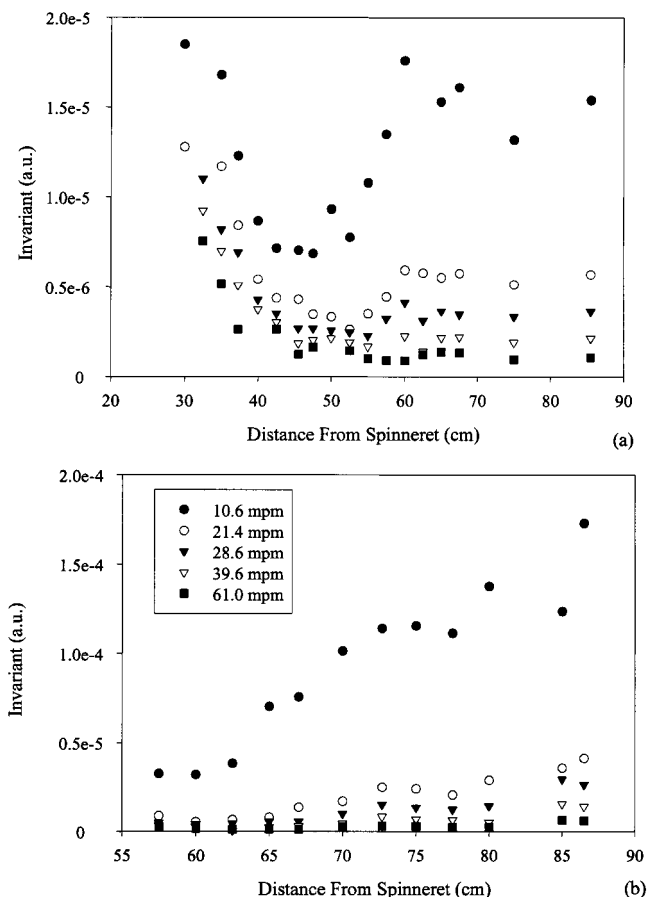
Figure 9. (a) Crystalline and (b) amorphous thicknesses of PVDF as calculated by the one-dimensional correlation function from the meridionally projected 2D SAXS data from the 2D wire detector.

Figure 10. Small-angle invariant for (a) PE and (b) PVDF as calculated from total scattered area under 2D wire detector data.

As the take-up speed is increased, the draw ratio increases and finer fibers are produced. The finer fibers release heat through their surface to the ambient environment more efficiently and thereby cool faster than do fibers spun at lower speeds. During this more rapid cooling, the volume element spends less time at higher temperatures, where the crystallization rate is relatively slow, and must then begin to crystallize at a lower temperature than would a thicker fiber. Thus, the crystallization onset temperature becomes lower as the take-up speed increases. It is well-known that crystal thickness decreases with decreasing crystallization temperature, in agreement with the findings here that the long period and crystalline lamellar thickness decrease with increasing take-up speed.

For all take-up speeds examined, there is an increase in amorphous thickness with take-up speed only in the case of PE. This is a result of the increased elongational stress accompanying the decreasing fiber diameter as take-up speed is increased. The rubbery PE amorphous segments have a much smaller tensile modulus than do the crystalline segments and therefore exhibit significant strain, while the crystalline regions are unaffected. PVDF does not exhibit these trends probably due to its stiffer characteristics.[38] The low-level stresses produced in this experiment are not of sufficient force to extend even the amorphous lamellae.

Figure 10 shows the small-angle invariant (total integrated area that may include equatorial streak and meridional streak (lobe)) as a function of take-up speed and distance from the spinneret for both PE and PVDF.

In the case of either polymer, lower take-up speeds correspond to greater invariant values, and vice versa. For each polymer studied, the specific trends with distance from the spinneret appear to be very different. For PE, the invariant begins at a high value then decreases for all take-up speeds examined. The invariant then reaches a minimum value. The invariant begins to increase again at the position where the onset of crystallization was observed in Figure 5. The invariant goes through a secondary maximum value and then remains at a steady value. The secondary rise is take-up speed dependent, with the low take-up speeds producing peaking at a level just below their initial maximum and the high take-up speeds barely increasing to a secondary maximum at all.

The PVDF invariant has a simpler dependence on spinneret distance. With increasing distance from the spinneret, the invariant increases in a nearly linear fashion. The invariant at low take-up speeds increases to nearly 2.5 times its original value, while the invariant at high take-up speeds barely increases at all. It appears that the changes of behavior of PVDF represent only the middle section of the invariant evolution in PE.

The initial high invariant for PE, arising from an equatorial streak and its subsequent decline, is intriguing. This scattering clearly arises from a long narrow entity which is aligned parallel to the fiber axis. At this time, the nature of this entity and the coupled phenomenon of its gradual disappearance just before the clear manifestation of crystallinity are conjectural. Two possibilities are (1) the formation and subsequent disappearance of rodlike entities precursory to observable
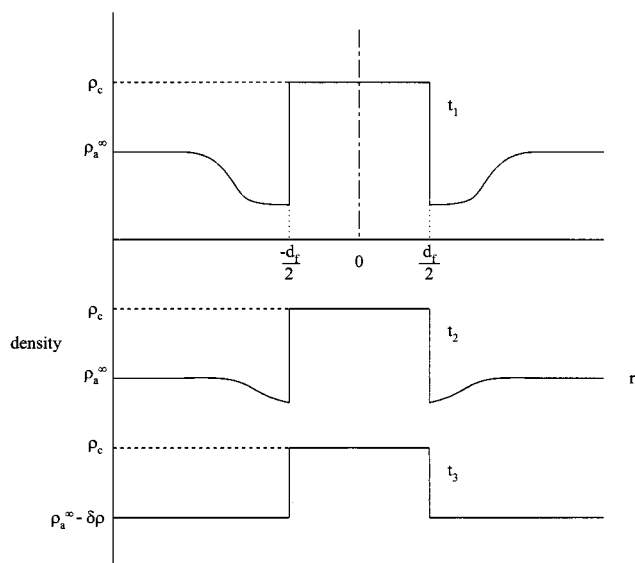
Figure 11. Schematic representation of the creation and subsequent elimination of a density-deficient volume surrounding a microfibril of diameter d_f. The figure shows density versus position at times $t_1 < t_2 < t_3$.

crystals or (2) the formation and subsequent healing of narrow, axial voids. In fact, both possibilities are related.

Rodlike precursors (or highly defective, microfibrillar crystallites) have been observed in TEM[39] and WAXS[40] and SAXS[41] studies of structure development in poly-(ethylene terephthalate) fibers. These microfibrillar entities occur in the earliest stage of crystallization under high orientation and are substantially supplanted by rows of lamellar crystals.[39] The presence of such microfibrils in PE fibers could directly explain the appearance of the equatorial streak. The subsequent gradual disappearance of the equatorial streak could then be a consequence of relaxation of the melt adjacent to the microfibrils. This relaxation of the melt would increase its entropy, thereby decreasing the melting point and force melting of the chains already in poor registry in the microfibrils. This explanation derives from a similar description by Hearle[42] of the instability of defective crystals in melt-spun fibers.

Consider now another aspect of the formation of the suggested microfibrils. The specific volume of the microfibril must be lower than that of the material from which it has formed. If time allowed, relaxation and migration of chains from the surroundings would smooth the density decrement about the just-formed fibril. However, if the microfibril formed rapidly, there could be a time interval in which the density deficit would remain localized about the microfibril, as depicted in Figure 11. This thin matter-deficient layer would amount to a "correlation hole" and would lead to a locally high electron density difference and thereby strong scattering. With time, at least the shorter chains will relax and migrate toward the microfibril interface, and the material deficit will gradually disappear and the scattering intensity will drop. Such a matter-deficient layer could indeed be the "longitudinal void" often suggested to explain equatorial streaking.

While there is no evidence toward either of these models, both are conceptually consistent with the occurrence and subsequent gradual disappearance of an equatorial streak and are presented in the spirit of fostering discussion of this phenomenon.

Alternatively, the decrease of the equatorial streak intensity could be a consequence of the initial shish structure having a higher electron density (close to the crystal density) than the surrounding amorphous phase; thus, the scattering contrast is high at the early stages. As crystallization develops, the electron density of the surrounding medium increases, which will decrease the contrast between the shishes and the surrounding lamellar kabobs.

The subsequent development of small-angle meridional lobes represents the formation of lamellar stacks. For PE the development of such stacks largely follows the elimination of the axial feature, giving rise to the equatorial streak. In this case, the small-angle invariant therefore drops before increasing with the development of the meridional lobes. For PVDF, the meridional lobes begin to form and amplify while the equatorial streak is disappearing, thereby producing a monotonically increasing invariant magnitude. Very likely, the higher relaxation time of PVDF has reduced the rate of relaxation that would be required to reduce the equatorial streak intensity by the proposed models.

Conclusions

In the present study, the melt spinning of PE and PVDF was studied using simultaneous in-situ small- and wide-angle synchrotron X-ray scattering. Structure and morphology development was studied as a function of distance from the spinneret and take-up speed. Careful analysis of scattering patterns was used to reinvestigate the kinetic difference between SAXS and WAXS signals.

The following conclusions were reached in examination of the present data:

(i) Upon careful examination, both PE and PVDF exhibited SAXS before WAXS behavior. However, detailed examination indicates that the equatorial streak occurs prior to the meridional streak (or lobe). This clearly favors the shish-kebob mechanism proposed by Keller et al.[31] These results do not favor the spinodal decomposition mechanism as a precursor of crystallization

(ii) The onset of crystallization was captured for both polymers and is a function of both take-up speed and distance from the spinneret.

(iii) PE and PVDF both exhibit shish-kebob-like morphology. The mechanism for the development of this morphology probably begins with the development of very defective shishlike crystals, which are aligned along the fiber axis. The kebobs grow at perpendicular directions to the shish at a later time. In the case of PE, the kebobs exhibit a helical twisting around the *b*-axis as seen in the WAXS patterns. The divergence from true perpendicular growth of the kebobs is stronger at slower take-up speeds and at distances closer to the spinneret. As kebob growth gets underway, the shish destruction seems apparent. Both polymers eventually exhibit two-lobe SAXS patterns along the meridian, which is indicative of a lamellar stacking arrangement.

(iv) PVDF morphology is less affected by small stress changes as compared to PE morphology changes.

References and Notes

(1) Carothers, W. H.; Hill, J. W. *J. Am. Chem. Soc.* **1932**, *54*, 1579.
(2) Chappel, F. P.; Culpin, M. F.; Gosen, R. G.; Tranter, T. C. *J. Appl. Chem.* **1964**, *14*, 12.
(3) Katayama, K.; Amano, T.; Nakamura, K. *Kolloid Z. Z. Polym.* **1968**, *226*, 125.
(4) Dees, J. R.; Spruiell, J. E. *J. Appl. Polym. Sci.* **1974**, *18*, 1055.
(5) Spruiell, J. E.; White, J. L. *Polym. Eng. Sci.* **1975**, *15*, 660.
(6) Nadella, H.; Henson, H. M.; Spruiell, J. E.; White, J. L. *J. Appl. Polym. Sci.* **1977**, *21*, 3013.
(7) Bankar, V.; Spruiell, J. E.; White, J. L. *J. Appl. Polym. Sci.* **1977**, *21*, 2341.
(8) Danford, M. D.; Spruiell, J. E.; White, J. L. *J. Appl. Polym. Sci.* **1978**, *22*, 3351.
(9) White, J. L.; Dharod, K. C.; Clark, E. S. *J. Appl. Polym. Sci.* **1974**, *18*, 2539.
(10) Nadkarni, V. N.; Schultz, J. M. *J. Polym. Sci., Polym. Phys. Ed.* **1977**, *15*, 2151.
(11) Hirahata, H.; Seifert, S.; Zachmann, H. G.; Yabuki, K. *Polymer* **1996**, *37*, 5131.
(12) Wang, Y.; Cakmak, M.; White, J. L. *J. Appl. Polym. Sci.* **1985**, *30*, 2615.
(13) Cakmak, M.; Teitge, A.; Zachmann, H. G.; White, J. L. *J. Polym. Phys., Polym. Phys.* **1993**, *31*, 371.
(14) Hsiao, B. S.; Barton Jr., R.; Quintana, J. *J. Appl. Polym. Sci.* **1996**, *62*, 2061.
(15) Bheda, J. H.; Spruiell, J. E. *J. Appl. Polym. Sci.* **1990**, *39*, 447.
(16) Samon, J. M.; Schultz, J. M.; Wu, J.; Hsiao, B. S.; Yeh, F.; Kolb, R. *J. Polym. Sci. Polym. Phys. Ed.* **1999**, *37*, 1277.
(17) White, J. L.; Cakmak, M. *Adv. Polym. Technol.* **1986**, *6*, 295.
(18) Kepler, R. G.; Anderson, R. A. *Adv. Phys.* **1992**, *41*, 1.
(19) Lovinger, A. J. *J. Polym. Sci., Polym. Phys. Ed.* **1980**, *18*, 793.
(20) Weinhold, S.; Litt, M. H.; Lando, J. B. *Macromolecules* **1980**, *13*, 1178.
(21) Matsushige, K.; Nagata, K.; Imada, S.; Takemura, T. *Polymer* **1980**, *21*, 1391.
(22) Doll, W. W.; Lando, J. B. *J. Macromol. Sci., Phys.* **1968**, *B2*, 219.
(23) Keller, A. *J. Polym. Sci.* **1955**, *15*, 31.
(24) Olmsted, P. D.; Poon, W. C. K.; McLeish, T. C. B.; Terrill, N. J.; Ryan, A. J. *Phys. Rev. Lett.* **1998**, *81*, 373.
(25) Elsner, G.; Riekel, C.; Zachmann, H. G. *Adv. Polym. Sci.* **1985**, *67*, 1.
(26) Gehrke, R.; Riekel, C.; Zachmann, H. G. *Polymer* **1989**, *30*, 1582.
(27) Strobl, G. R.; Schneider, M. *J. Polym. Sci., Polym. Phys.* **1980**, *18*, 1343.
(28) Russell, T. In *Handbook on Synchrotron Radiation*; Brown, G., Moncton, D. E., Eds.; Elsevier Science: New York, 1991; Vol. 3, Chapter 11, p 379.
(29) Hsiao, B. S.; Sauer, B. S.; Verma, R. K.; Zachmann, H. G.; Seifert, S.; Chu, B.; Harney, P. *Macromolecules* **1995**, *20*, 6931.
(30) Barrett, C. S.; Massalski, T. B. In *Structure of Metals*; McGraw-Hill: New York, 1966; Chapter 2, pp 30−50.
(31) Keller, A.; Kolnaar, H. W. K. In *Materials Science and Technology, A Comprehensive Treatment*; VCH: New York, 1997; Vol. 18, Chapter 4, p 190.
(32) Schultz, J. M.; Petermann, J. *Colloid Polym. Sci.* **1984**, *262*, 294.
(33) Imai, M.; Kaji, K.; Kanaya, T. *Macromolecules* **1994**, *27*, 7103.
(34) Terrill, N. J.; Fairclough, P. A.; Towns-Andrews, E.; Komanschek, B. U.; Young, R. J.; Ryan, A. J. *Polymer* **1998**, *39*, 2381.
(35) Ezquarra, T. A.; López-Cabarcos, E.; Hsiao, B. S.; Baltà-Calleja, F. J. *Phys. Rev. E* **1996**, *54*, 989.
(36) Petermann, J.; Gohil, R. M.; Schultz, J. M.; Hendricks, R. W.; Lin, J. S. *J. Polym. Sci., Polym. Phys. Ed.* **1982**, *20*, 523.
(37) Strobl, G. In *The Physics of Polymers*; Springer: Berlin, 1996; pp 173−176.
(38) Krisher, A. S.; Siebert, O. W. In *Perry's Chemical Engineers' Handbook*, 6th ed.; Perry, R. H., Green, D., Eds.; McGraw-Hill: New York, 1984; Chapter 23, pp 54−55.
(39) Chang, H.; Lee, K. G.; Schultz, J. M. *J. Macromol. Sci., Phys.* **1994**, *B33*, 105.
(40) Hristov, H. A.; Schultz, J. M. *J. Polym. Sci., Polym. Phys. Ed.* **1990**, *28*, 1647.
(41) Peszkin, P. N.; Schultz, J. M.; Lin, J. S. *J. Polym. Sci., Polym. Phys. Ed.* **1986**, *24*, 2591.
(42) Hearle, J. W. S. *J. Appl. Polym. Sci., Appl. Polym. Symp.* **1977**, *31*, 137.